Modelling dynamic changes in blood flow and volume in the cerebral vasculature

SJ Payne* and WK El-Bouri

Institute of Biomedical Engineering, Department of Engineering Science, University of Oxford

Parks Road, Oxford OX1 3PJ, UK

stephen.payne@eng.ox.ac.uk; wahbi.el-bouri@eng.ox.ac.uk

*Corresponding author

Conflicts of interest: none

WKEB was funded by an EPSRC Doctoral Training Partnership studentship, grant reference EP/M50659X/1.

Keywords: Cerebral blood flow; cerebral blood volume; vasculature; multiscale

Abstract

The cerebral microvasculature plays a key role in the transport of blood and the delivery of nutrients to the cells that perform brain function. Although recent advances in experimental imaging techniques mean that its structure and function can be interrogated to very small length scales, allowing individual vessels to be mapped to a fraction of 1 µm, these techniques currently remain confined to animal models. In-vivo human data can only be obtained at a much coarser length scale, of order 1 mm, meaning that mathematical models of the microvasculature play a key role in interpreting flow and metabolism data. However, there are close to 10,000 vessels even within a single voxel of size 1 mm^3. Given the number of vessels present within a typical voxel and the complexity of the governing equations for flow and volume changes, it is computationally

challenging to solve these in full, particularly when considering dynamic changes, such as those found in response to neural activation.

We thus consider here the governing equations and some of the simplifications that have been proposed in order more rigorously to justify in what generations of blood vessels these approximations are valid. We show that two approximations (neglecting the advection term and assuming a quasi-steady state solution for blood volume) can be applied throughout the cerebral vasculature and that two further approximations (a simple first order differential relationship between inlet and outlet flows and inlet and outlet pressures, and matching of static pressure at nodes) can be applied in vessels smaller than approximately 1 mm in diameter. We then show how these results can be applied in solving flow fields within cerebral vascular networks providing a simplified yet rigorous approach to solving dynamic flow fields and compare the results to those obtained with alternative approaches. We thus provide a framework to model cerebral blood flow and volume within the cerebral vasculature that can be used, particularly at sub human imaging length scales, to provide greater insight into the behaviour of blood flow and volume in the cerebral vasculature.

1 Introduction

Since 2006 there has been a great deal of interest in models of the cerebral microcirculation. This has been driven by the recent ability to obtain experimental data about microvascular networks, both in humans and in animal models. The former has mainly been based on the collection of post-mortem casts obtained by Duvernoy et al. (1981), and these experimental data have been presented in detail by Cassot et al. (2006), Lauwers et al. (2008) and Lorthois et al. (2011). Casts of animal microvascular networks have also been extracted and the flow in them modelled, see for example Fang et al. (2008), Weber et al. (2008), Reichold et al. (2009), Tsai et al. (2009), Guibert et al. (2010), Blinder et al. (2010), Safaeian et al. (2011), Kasische et al. (2011), Linninger et al. (2013), Gagnon et

al. (2015), Gould et al. (2017) and Schmid et al. (2017). Many of the models listed above have also examined the transport of oxygen and the coupling between this and cerebral blood flow.

Although there has been a great deal of progress on robustly extracting vascular networks from imaging data and converting them into accurately segmented three-dimensional networks, see for example Gould et al. (2017), acquiring large volumes of such data remains a time-consuming and expensive task that can only be undertaken with considerable expertise. The strong dependence of vessel resistance on vessel radius means that accurate values of the vessel diameter are critical if the flow field is to be calculated accurately. The strong dependence of the chosen boundary conditions on the flow simulations has also been noted by many authors, for example Lorthois et al. (2011).

These factors, together with the high vessel density that means that solving the flow field in volumes of tissue that are of the length scale of a human imaging voxel (of order 1 mm) is highly computationally challenging, has driven the development of homogenisation techniques based on the creation of artificial networks that match experimentally measured properties, Su et al. (2012), El-Bouri and Payne (2015) and El-Bouri and Payne (2016), and coupling these with models over multiple length scales, El-Bouri and Payne (2018). These techniques enable a scaling up of networks to a voxel scale and hence the flow fields can be related to imaging data, most easily through the use of transit time distributions, see for example Park and Payne (2013). Other authors have developed vascular networks through the use of bifurcating vessels, for example Boas et al. (2008) and Payne and Lucas (2017), although in these models no spatial information is considered.

At a voxel level, the vasculature comprises vessels over a relatively wide range of length scales, with diameters ranging from a few micrometres to hundreds of micrometres. Consideration does thus need to be given to the assumptions and choice of equations that govern blood flow over these length scales, in particular when attempting to bridge the ‘imaging gap’, when the assumptions valid in the large vessels and those in the microvasculature may be significantly different. At the smallest length scales, nearly all authors use the Poiseuille equation in some form, with viscosity either taken

to be constant, based on vessel diameter or based on vessel diameter and haematocrit, as shown in Table 1. In the latter two cases, empirical relationships are normally used, with a variety of different relationships having been applied. Once the resistance to flow is known, then the network reduces to a conductance matrix, which can be solved numerically, either by simple inversion for networks with constant haematocrit or by iteration for networks with non-constant haematocrit. It is usually assumed that at small length scales static pressure is conserved at nodes, as has been done in all the studies listed thus far.

Most of the models listed in Table 1 assume steady state flow conditions, with only a few considering the dynamic response, although this plays an important part in interpreting the response to changes in neural activity. Only the models by Boas et al. (2008), Reichold et al. (2009), Gagnon et al. (2015) and Payne and Lucas (2017) consider the dynamic response of the small vessels in the cerebral vasculature. These mostly assume a non-linear compliance of the vessels, enabling changes in flow to drive changes in volume. Such changes in blood volume are of particular importance in the context of imaging techniques such as the BOLD response, where short-term changes in blood volume can strongly influence the response.

Model	**Static/dynamic**	**Flow model**	**Viscosity model**
Fang et al. (2008)	Static	Poiseuille equation	Constant
Boas et al. (2008)	Dynamic	Poiseuille equation and non-linear compliance	Pries et al. (1992), with haematocrit as function of diameter
Reichold et al. (2009)	Dynamic	Poiseuille equation and non-linear compliance	Pries et al. (1992), with haematocrit as function of diameter
Guibert et al.	Static	Poiseuille equation	Kiani and Hudetz (1991) or Pries

(2010)			and Secomb (2005), with haematocrit model
Lorthois et al. (2011)	Static	Poiseuille equation	Pries et al. (1996), with haematocrit model
Safaeian et al. (2011)	Static	Poiseuille equation	Pries and Secomb (2005), with haematocrit model
Linninger et al. (2013)	Static	Poiseuille equation	Pries et al. (1996), with constant haematocrit
Gagnon et al. (2015)	Dynamic	Poiseuille equation and non-linear compliance	Pries et al. (1990), 'corrected for haematocrit'
Gould et al. (2017)	Static	Coupled model of flow and haematocrit, rigid vessels	Plasma skimming model
Schmid et al. (2017)	Static	Poiseuille equation	Pries et al. (1992), with tracking of red blood cells
Payne and Lucas (2017)	Dynamic	Poiseuille equation	Pries et al. (1992), with constant haematocrit
El-Bouri and Payne (2018)	Static	Poiseuille equation	Pries et al. (1992), with constant haematocrit

Table 1 Summary of network models of cerebral blood flow and assumptions used

Other approaches have taken a more 'top-down' methodology, where lumped parameter models (e.g. windkessel models) are used, with the lumped parameters aiming to capture the overall behaviour of flow through large numbers of vessels in a very small number of parameters, see for example those used by Ress et al. (2009), Kim et al. (2013) in the context of models of oxygen delivery, and Buxton et al. (1998) and many subsequent studies (for example Aquino et al. (2014)) in the context of models of the BOLD response. Such models have a valuable role to play in

understanding the behaviour at large scales, but are inevitably limited by both their simplicity and the difficulties involved in linking the model parameters to the underlying network physiology.

The assumptions made are often very different in models of flow in the larger vessels, for example when the dynamic behaviour of the flow field plays an important part in both flow and volume, and when total pressure is often conserved at nodes, see for example Alastruey et al. (2007). In order to link models across the 'imaging gap', care has to be taken and the limits of assumptions fully understood. For a comprehensive review of models of cerebral blood flow, the reader is referred to Payne (2017).

In this paper we thus consider the modelling of cerebral blood flow and volume in networks of blood vessels in detail, justify suitable approximations that can be made, and propose a framework that can be used that is mathematically rigorous and computationally simple. We will also consider the limits of the approximations and hence illustrate how models can be developed that will cover multiple scales. In order to do this, we consider the governing equations and use these to develop a model relating blood flow and volume to pressure in a single vessel; finally we link vessels together within a network and then show how the equations can be solved dynamically within a network. In the last section we will consider each of these in turn before illustrating our proposed approach in the context of the cerebral vasculature, comparing simulation results with those obtained using previous approaches.

2 Theory

We assume blood to be a Newtonian fluid of viscosity μ and density ρ in a flow field that is governed by the incompressible form of the Navier-Stokes equations. These fundamental fluid flow equations are based on the concepts of conservation of mass and balance of forces; a full explanation and derivation can be found in many sources, see for example Acheson (1990). Hence:

$$\frac{\partial \mathbf{u}}{\partial t} + (\mathbf{u}.\nabla)\mathbf{u} = -\frac{1}{\rho}\nabla p + \frac{\mu}{\rho}\nabla^2\mathbf{u} \quad (1)$$

with velocity field **u** driven by a pressure field *p*. In an axisymmetric vessel this reduces to:

$$\frac{\partial u}{\partial t} + u\frac{\partial u}{\partial x} = -\frac{1}{\rho}\frac{\partial p}{\partial x} + \frac{\mu}{\rho}\nabla^2 u \quad (2)$$

where the flow velocity has only an axial component, *u*, which is a function of radius, *r*, axial position, *x*, and time, *t*. In this latter case, the pressure gradient can be shown to be only a function of axial position and time, i.e. the pressure is uniform over the cross-sectional area, based on order of magnitude arguments, Canic and Kim (2003). A similar order of magnitude argument can be used to neglect the radial component of the velocity field when the variations in the vessel cross-section are not too fast, Canic and Kim (2003). We note that the assumption of a Newtonian fluid is a limitation to this analysis, but one that we will consider more fully in the Discussion. For ease of reference, schematics of the different components of the model are shown in Figure 1, to which we refer throughout.

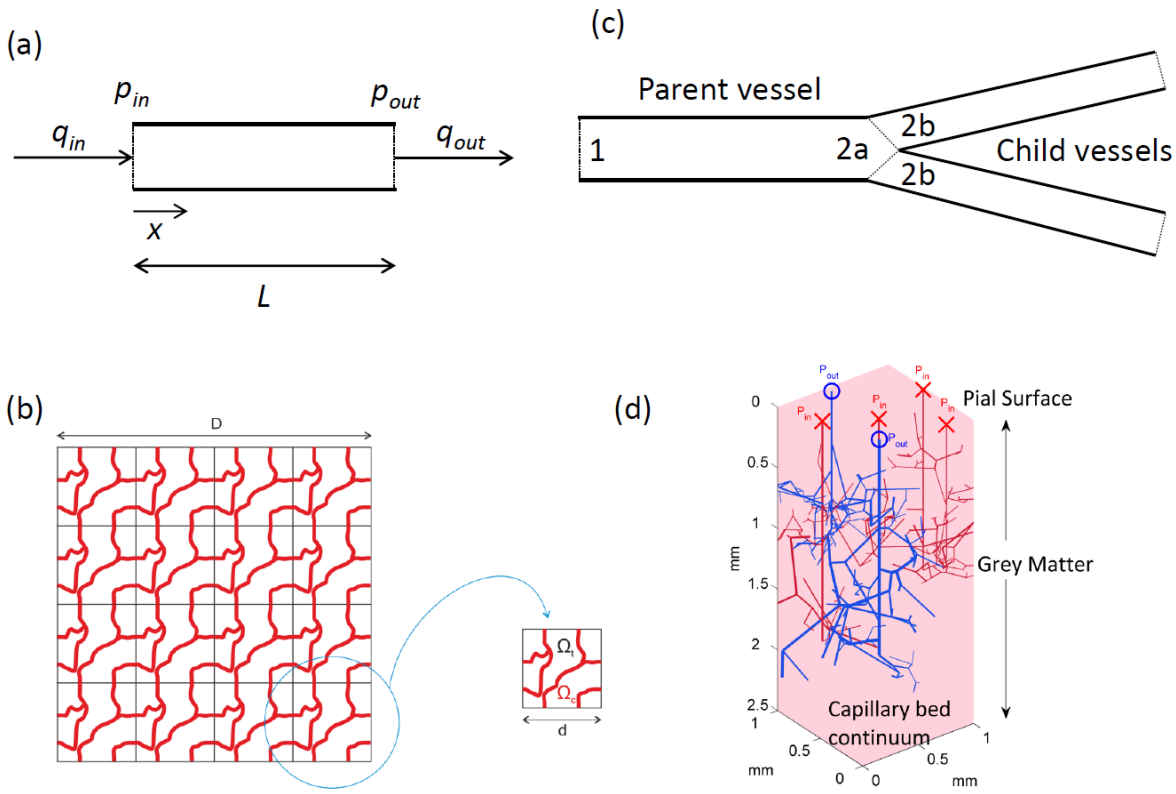

Figure 1 Schematic of components of model: (a) single vessel model; (b) continuum model; (c) node model; (d) coupled penetrating vessel and capillary bed continuum model. Figures (b) and (d) reproduced from El-Bouri (2017)

2.1 Result 1: The advection term can be neglected when $\frac{E}{\rho U^2}\frac{h}{R} \gg \frac{3}{2}$ (*E* is Young's modulus, *ρ* is fluid density, *U* is flow velocity, *h* is wall thickness and *R* is vessel inner radius)

The first result that we show is that the advection term can be neglected in models of cerebral blood flow when the vessel wall stiffness scaled by wall thickness to radius ratio is greater than a multiple of the dynamic head. This result is required first to enable us to write down the governing equations in a simplified form so that we can derive a model for the inlet and outlet flows in the next section.

We will demonstrate this in two parts. We first consider the flow in individual vessels, Figure 1a, since a simple result can be obtained, before considering the flow field across multiple scales, Figure 1b. This latter approach allows us to consider the flow field as a whole; this is valuable since it links to previous work that has shown how the flow field in the capillary vessels can be modelled using homogenisation, El-Bouri and Payne (2015). For simplicity we only consider the steady state solution, but this does not affect the result.

Single vessels

We firstly reduce the steady state form of Equation 2 to non-dimensional form, where we reference velocity and pressure to characteristic values, *U* and *P* respectively:

$$u^*\frac{\partial u^*}{\partial x^*} = -\left(\frac{P}{\rho U^2}\right)\frac{\partial p^*}{\partial x^*} + \frac{1}{Re_L}\nabla^2 u^* \quad (3)$$

where the star is used here to denote a value as a fraction of its characteristic value, i.e. $u^* = u/U$, $p^* = p/P$ and $x^* = x/L$, and noting that we do not assume any relationship between characteristic pressure and characteristic velocity, retaining generality at this stage. The co-ordinate *x* is

referenced to vessel length, L (and hence the ∇^2 operator is also made non-dimensional with respect to L). Note that Reynolds number in Equation 3 is based on vessel length:

$$Re_L = \frac{\rho U L}{\mu} \quad (4)$$

We use a subscript for Reynolds number throughout to make it clear what length scale is being used. The aim is then to consider the relative magnitudes of the advection and pressure gradient terms, since these are the two terms with first order axial derivative terms and thus terms that can be compared directly through order of magnitude arguments.

Conservation of mass, averaged over the cross-sectional area, gives:

$$\frac{\partial A}{\partial t} + \frac{\partial q}{\partial x} = 0 \quad (5)$$

where the flow rate, q, is the integral of the axial velocity over the cross-sectional area: see Canic and Kim (2003) for a formal derivation of this result. In the steady state this reduces to a flow rate that is invariant over axial length, as expected. Hence:

$$A = \frac{q}{\overline{U}} \quad (6)$$

where the area-averaged velocity is given by $\overline{U}$ (which can vary along the vessel). We next assume that a relationship can be formulated between steady state pressure and cross-sectional area (without at this stage specifying its form), i.e. $p = p(A)$. We neglect any viscous component of the wall response here as we are only considering the steady state behaviour: note, however, that we retain the viscous behaviour of the fluid, which means that the pressure will drop in the direction of flow and hence the cross-sectional area of the vessel will also change in order to maintain flow rate. We also neglect any axial stiffness, only considering the radial stiffness, as is commonly done, for simplicity.

Using this assumption, Equations 3 and 6 yields:

$$u^* \frac{\partial u^*}{\partial x^*} = \left[A \frac{dp}{dA} \left(\frac{1}{\rho U^2} \right) \frac{U}{\overline{U}} \right] \frac{\partial \overline{U}^*}{\partial x^*} + \frac{1}{Re_R (R/L)} \nabla^2 u^* \quad (7)$$

where Reynolds number in Equation 7 is now based on vessel radius and this is scaled by the ratio of vessel radius to length (R/L). The key parameter is then the square bracket, since if this is much larger than 1, the advection term can be neglected in comparison with the pressure gradient term (note that although the derivatives are of different velocity terms, one being velocity as a function of radius and one the area-averaged velocity, they are of the same order of magnitude).

We therefore need to consider the pressure-area relationship more closely. Many different forms have been proposed for this, for example those by Langewouters et al. (1984), Stergiopoulos et al. (1992) and Formaggia et al. (1999). For simplicity we use the relationship that results from assuming static radial equilibrium of an isotropic elastic material with Young's modulus *E*, Poisson ratio ν,reference wall thickness h_{ref} and radius R_{ref}, as quoted by Formaggia et al. (1999) and widely used elsewhere:

$$p - p_{ref} = \frac{E h_{ref}}{R_{ref}(1 - \nu^2)} \left(\sqrt{\frac{A}{A_{ref}}} - 1 \right) \quad (8)$$

where the wall stiffness relates changes in pressure relative to a reference value, p_{ref}, to changes in cross-sectional area relative to a reference value, $A_{ref} = \pi R_{ref}^2$. Note that this model assumes that there is no axial stiffness: the wall thus responds at each axial location to the pressure at that location without reference to the remainder of the pressure field. More sophisticated models have been used, see for example Pedrizzetti and Perktold (2003), but this assumption is very commonly made in models of blood flow and is sufficient for the order of magnitude argument being made here.

This then gives:

$$\left[A\frac{dp}{dA}\left(\frac{1}{\rho U^2}\right)\frac{U}{\overline{U}}\right] = \frac{1}{2}\frac{E}{\rho U^2}\frac{h_{ref}}{R_{ref}(1-\nu^2)}\sqrt{\frac{A}{A_{ref}}}\frac{U}{\overline{U}} \quad (9)$$

Since we can select the characteristic velocity to be close to the area-averaged value and assuming that all values are close to their reference value, this simplifies to give:

$$\left[A\frac{dp}{dA}\left(\frac{1}{\rho U^2}\right)\frac{U}{\overline{U}}\right] \approx \frac{2}{3}\frac{E}{\rho U^2}\frac{h}{R} \quad (10)$$

where we also assume a value of Poisson ratio of 0.5, denoting an incompressible material, as is commonly done. For advection to be neglected, this term must be significantly greater than 1, hence $\frac{E}{\rho U^2}\frac{h}{R} \gg \frac{3}{2}$. We will examine this result again in the context of the cerebral vasculature later.

Note that although we have only considered the steady state response here, the result is also valid for dynamic flow fields, since we have compared the two terms with first order axial derivatives and thus including dynamic terms in the equations will not affect the validity of this particular result. It would be worth considering in future the relative magnitudes of the acceleration term and the viscous wall behaviour (the two terms with first order time derivatives). It should be noted, however, that the available data for visco-elastic models of the vessel wall in the cerebral vasculature are very sparse.

Continuous flow field

Having considered the flow in individual vessels above, we next show how the advection term can be neglected when considering the flow field as a continuous one. This approach is based on the method set out by Shipley and Chapman (2010) and previously adapted for the cerebral microcirculation by El-Bouri and Payne (2015). We include this analysis since we have previously shown how the flow field within volumes of brain tissue can be modelled using a coupled approach that incorporates both the flow in individual non-capillary vessels and a Darcy flow for the capillary

vessels, El-Bouri and Payne (2018), and thus wish to show that the advection term can be neglected when considering the flow field as a continuum.

As before, we consider the solution in the steady state but start from the Navier-Stokes equations for incompressible flow:

$$(\mathbf{u}_c.\nabla)\mathbf{u}_c = -\frac{1}{\rho}\nabla p_c + \frac{\mu}{\rho}\nabla^2\mathbf{u}_c \; in \; \Omega_c \; (11)$$

where the velocity field in the capillary domain, Ω_c, is given by $\mathbf{u}_c$. The boundary conditions are as given in El-Bouri and Payne (2015): however, since we are not attempting to solve the equations here, we will not consider the boundary conditions further as they are not directly relevant to the derivation below. We define a small parameter $\varepsilon = d/D$ that relates the micro length scale, *d*, to the macro length scale, *D*, as shown in Figure 1b (note that this definition of ε is only used in this section).

We reduce the equations to non-dimensional form using the following scaling:

$$\mathbf{u}_c = U\mathbf{u}_c^* \; (12)$$

$$p = \frac{\mu D U}{d^2}p^* + p_0 \; (13)$$

$$\mathbf{X} = d\mathbf{X}^* \; (14)$$

based on a characteristic velocity *U*, capillary length scale *d*, voxel length scale *D*, and a characteristic pressure that is based on viscous forces with an arbitrary offset. This scaling of pressure is based on the fact that viscous forces dominate at the local scale and thus to bring the characteristic value of pressure to the macro scale it is rescaled by ε^{-2}: this is due to the fact that the inter-capillary spacing is of order ε and so there are of order ε^2 capillaries per unit area, meaning that pressure scales with ε^{-2}. These characteristic values reduce Equation 11 to the following (where we drop the star notation straight away for ease of notation):

$$\varepsilon Re_d(\mathbf{u}_c.\nabla)\mathbf{u}_c = -\nabla p_c + \varepsilon\mu\nabla^2\mathbf{u}_c \ (15)$$

where Reynolds number on the micro scale is defined as:

$$Re_d = \frac{\rho U d}{\mu} \ (16)$$

and the Reynolds number on the macro scale is therefore equal to $Re_D = Re_d/\varepsilon$. Since the problem is more commonly formulated in terms of this parameter, Equation 15 thus becomes:

$$\varepsilon^2 Re_D(\mathbf{u}_c.\nabla)\mathbf{u}_c = -\nabla p_c + \varepsilon\mu\nabla^2\mathbf{u}_c \ (17)$$

Since we consider the capillary bed relative to the larger vessels here, this gives micro and macro length scales of approximately 100 µm and 1 cm respectively (noting that this analysis can be applied to any separation of scales where the parameter ε is small). In this case, this parameter is equal to approximately 0.01. For typical values of blood viscosity and density (3 mPa.s and 1040 kg/m^3 respectively), the macro Reynolds number is of order 1, where we assume a capillary velocity of order 1 mm/s, see for example Unekawa et al. (2010). There is thus no need to re-scale Equation 17.

We now use a classical separation of scales approach. Since $\varepsilon \ll 1$, the local and macro length scales are well separated and can be defined as $\mathbf{X}$ and $\mathbf{x} = \varepsilon\mathbf{X}$. Hence, using the standard approach, see for example Holmes (2013), for separation of scales:

$$\nabla = \nabla_X + \varepsilon\nabla_x \ (18)$$

$$\nabla^2 = \nabla_X^2 + 2\varepsilon\nabla_x.\nabla_X + \varepsilon^2\nabla_x^2 \ (19)$$

and a multiple scales expansion:

$$\mathbf{u}_c = \mathbf{u}_c^0(\mathbf{x},\mathbf{X}) + \varepsilon\mathbf{u}_c^1(\mathbf{x},\mathbf{X}) + \varepsilon^2\mathbf{u}_c^2(\mathbf{x},\mathbf{X}) + \cdots \ (20)$$

$$p = p^0(\mathbf{x},\mathbf{X}) + \varepsilon p^1(\mathbf{x},\mathbf{X}) + \varepsilon^2 p^2(\mathbf{x},\mathbf{X}) + \cdots \ (21)$$

Substituting Equations 18-21 into the governing equation (Equation 17) orders of ε can now be compared.

First in ε^0:

$$\nabla_X p^0 = 0 \ (22)$$

and then in ε^1:

$$\nabla_X p^1 + \nabla_x p^0 = \nabla_X^2 \mathbf{u}_c^0 \ (23)$$

Equations 22 and 23 can be solved along the lines proposed by Shipley and Chapman (2012) and as performed in the cerebral microvasculature by El-Bouri and Payne (2015): these two equations are sufficient to solve to leading order. The full derivation is given in Appendix A, with the end result being a volume-averaged Darcy equation:

$$\langle \mathbf{u}_c^{(0)} \rangle_{\Omega_c} = -\mathbf{K} \nabla_x p_c^{(0)} \ (24)$$

where the permeability tensor, $\mathbf{K}$, is given in full in Appendix A. The advection term thus plays no role in this context at leading order and can be considered only as a small correction term.

These two results thus combine to show that the advection term can be neglected in both individual vessels (under the condition given above) and in the microvasculature when treated as a continuum. This is a very important result, as it removes the only non-linear term in the Navier-Stokes equations. Based on this result, we can utilise a wide range of results based on linear theory. It is worth noting in passing that a number of authors have neglected the advection term by linearizing the governing equations about a zero mean velocity, see for example Flores et al. (2016). Although the final result obtained is the same, this linearization is, strictly speaking, unnecessary and can appear to limit the validity of the solution. The results above offer a more rigorous and general proof that has a simple condition: one that we will examine in more detail in the context of the cerebral circulation later.

2.2 Result 2: A first order differential model relating inlet and outlet flows to inlet and outlet pressures in a vessel can be used when $\alpha < 1$ (α is Womersley number)

Having considered the flow as continuous in the second half of the result above, we now return to consideration of a single vessel, as shown in Figure 1a. The aim here is to solve for the flow field such that a relationship can be derived between the inlet and outlet flows and the inlet and outlet pressures. In this way a simple relationship can be used for the flow in and out of each vessel in a network such that a network of vessels can be connected together, using the results presented later.

In Result 1, we showed that the advection term can be neglected. As a result the governing equations for flow in a single compliant vessel (the area-averaged Navier-Stokes equations coupled with an elastic wall model) reduce to a linear form, enabling them to be transformed into the frequency domain and written in the following form:

$$\hat{p}'' = \left(\frac{i\omega ZC}{L^2}\right)\hat{p} \quad (25)$$

where:

$$Z = \mathcal{R}\frac{i\alpha^2}{8}\left[1 - \frac{2}{\alpha i^{3/2}}\frac{J_1(\alpha i^{3/2})}{J_0(\alpha i^{3/2})}\right]^{-1} \quad (26)$$

and impedance, Z, resistance, $\mathcal{R}$, and compliance, C, are defined here for the whole vessel, of length L . J_0 and J_1 denote Bessel functions of the first kind. We omit the dependence on frequency for clarity, since the overhat denotes that the variable has been transformed into the frequency domain. Womersley number is denoted by $\alpha = R\sqrt{\omega/\nu}$ and can be considered to be the ratio of oscillatory inertial forces to shear forces. The derivation for these equations is based on the results of Womersley (1955) and can be found in full in Flores et al. (2016). A schematic of the single vessel model is shown in Figure 1a: we now consider this single vessel in this section without further reference to the continuum model.

We can then use a perturbation series for pressure:

$$\hat{p} = \hat{p}_0 + \varepsilon\hat{p}_1 + \varepsilon^2\hat{p}_2 \dots (27)$$

in the small parameter, ε, defined in this section as:

$$\varepsilon = \alpha i^{3/2} \ (28)$$

We will examine the magnitude of this parameter later, but note that for the moment we are simply assuming that it has magnitude less than one. Note that this is a different definition for ε from that used in Section 2.1: we use this definition here as it is the standard notation for perturbation methods and thus enables results obtained here to be easily compared with equivalent results elsewhere.

Substituting Equation 28 into Equation 26 and Equations 26 and 27 into Equation 25 then yields:

$$[\varepsilon J_0(\varepsilon) - 2J_1(\varepsilon)](\hat{p}_0'' + \varepsilon\hat{p}_1'' + \varepsilon^2\hat{p}_2'' \dots) = \varepsilon^5\left(\frac{\nu\mathcal{R}C}{8L^2R^2}\right)J_0(\varepsilon)(\hat{p}_0 + \varepsilon\hat{p}_1 + \varepsilon^2\hat{p}_2 \dots) \ (29)$$

We next convert the variables to non-dimensional form, such that pressure is computed relative to a reference value (the value of this is irrelevant, since both sides of Equation 29 are linearly proportional to pressure) and length relative to the length of the vessel, L. The prime thus becomes relative to fractional length along the vessel. The problem is then defined in just two parameters, ε, and:

$$\beta = \frac{\nu\mathcal{R}C}{8R^2} \ (30)$$

where resistance and compliance are equal to:

$$\mathcal{R} = \frac{8\mu L}{\pi R^4} \ (31)$$

$$C = L\frac{dA}{dp} \ (32)$$

The non-dimensional parameter β is of similar form to the (inverse square of) Womersley number, but based on the time constant of the vessel (where $T = \mathcal{R}C$, as defined later) rather than the oscillation frequency. The behaviour of each vessel is thus governed by the relative magnitudes of these two non-dimensional groups.

To calculate the pressure series, we next use the series expansion of the Bessel functions, Abramowitz and Stegun (1964):

$$J_0(x) = \sum_{i=0}^{\infty} \frac{(-1)^k}{2^{2k}(k!)^2} x^{2k} = 1 - \frac{x^2}{4} + \frac{x^4}{64} - \frac{x^6}{2304} + \cdots \quad (33)$$

$$J_1(x) = \sum_{i=0}^{\infty} \frac{(-1)^k}{2^{2k+1} k!\,(k+1)!} x^{2k+1} = \frac{x}{2} - \frac{x^3}{16} + \frac{x^5}{384} - \frac{x^7}{18432} + \cdots \quad (34)$$

Balancing terms in ascending powers of ε gives:

$$\hat{p}_0'' = 0 \quad (35)$$

which means that the pressure field to zeroth order is linear, set by the inlet and outlet boundary conditions, as would be expected;

$$\hat{p}_1'' = 0 \quad (36)$$

which means that the first order pressure field is zero everywhere, since the inlet and outlet boundary conditions at first and higher orders are zero;

$$\hat{p}_2'' = -8\beta\hat{p}_0 \quad (37)$$

which can be solved as described below;

$$\hat{p}_3'' = 0 \quad (38)$$

which means that the third order pressure field is also zero everywhere; and

$$\hat{p}_4'' = -8\beta\left[\hat{p}_2 - \frac{1}{6}\hat{p}_0\right] \quad (39)$$

We can now proceed to solve for the pressure field in the vessel up to this order. Equation 35 can be solved using the inlet and outlet boundary conditions, defined here to be:

$$\hat{p}_0(x=0) = \hat{p}_{in} \quad (40)$$

$$\hat{p}_0(x=1) = \hat{p}_{out} \quad (41)$$

noting that these boundary conditions can of course be dynamically varying, since this is the solution in the frequency domain, which can easily be inverted into the time domain. The zeroth order pressure field is:

$$\hat{p}_0 = \hat{p}_{in}(1-x) + \hat{p}_{out}x \quad (42)$$

The resulting second order expression is calculated by substitution of Equation 42 into Equation 37 and solving given zero boundary conditions:

$$\hat{p}_2 = \hat{p}_{in}\frac{4\beta}{3}x(1-x)(2-x) + \hat{p}_{out}\frac{4\beta}{3}x(1-x^2) \quad (43)$$

and the fourth order expression similarly using Equations 42, 43 and 39:

$$\hat{p}_4 = -8\beta\left[\hat{p}_{in}x(1-x)\left\{-\frac{\beta}{45}(3x^3 - 12x^2 + 8x - 8) + \frac{1}{36}(2-x)\right\}\right.$$
$$\left. + \hat{p}_{out}x(1-x)\left\{\frac{\beta}{45}(3x^3 + 3x^2 - 7x - 7) + \frac{1}{36}(1+x)\right\}\right] \quad (44)$$

The full solution is then:

$$\hat{p} = \hat{p}_0 + \varepsilon^2\hat{p}_2 + \varepsilon^4\hat{p}_4 \ldots (45)$$

It should be noted that the expansion has been performed in terms of ε, but gives an expansion in terms of even powers of ε, where ε is proportional to the square root of frequency: hence the expansion is in integer powers of frequency.

Given the solution for the pressure field in the vessel, the flow field in the vessel can be calculated. This is most easily done using a second perturbation series for flow of the form:

$$\hat{q} = \hat{q}_0 + \varepsilon\hat{q}_1 + \varepsilon^2\hat{q}_2 \dots (46)$$

where we substitute this into the expression for impedance:

$$\hat{q} = -\frac{1}{Z}\hat{p}' \ (47)$$

where the impedance is given by Equation 26 and the pressure by Equation 45, to obtain an expression along the lines of Equation 29. We then calculate the flow field by balancing terms in powers of ε, as done for the pressure field earlier, to give:

$$\hat{q}_0 = -\frac{1}{\mathcal{R}}\hat{p}_0' \ (48)$$

$$\hat{q}_2 = -\frac{1}{\mathcal{R}}\left[\hat{p}_2' + \frac{1}{6}\hat{p}_0'\right] \ (49)$$

$$\hat{q}_4 = -\frac{1}{\mathcal{R}}\left[\hat{p}_4' + \frac{1}{6}\hat{p}_2' + \frac{11}{384}\hat{p}_0'\right] \ (50)$$

where the differentials are again relative to non-dimensional length. Equations 42-44 can then be substituted into these equations to derive an expression for the whole flow field. Most usefully, however, the inlet and outlet flows can be calculated in terms of the inlet and outlet pressures. Since these are linear, they are most easily written in matrix form:

$$\begin{pmatrix} \hat{q}_{in} \\ \hat{q}_{out} \end{pmatrix} = \boldsymbol{\alpha}_0 \begin{pmatrix} \hat{p}_{in} \\ \hat{p}_{out} \end{pmatrix} + \boldsymbol{\alpha}_2\varepsilon^2 \begin{pmatrix} \hat{p}_{in} \\ \hat{p}_{out} \end{pmatrix} + \boldsymbol{\alpha}_4\varepsilon^4 \begin{pmatrix} \hat{p}_{in} \\ \hat{p}_{out} \end{pmatrix} + \cdots \ (51)$$

where:

$$\boldsymbol{\alpha}_0 = \frac{1}{\mathcal{R}}\begin{pmatrix} 1 & -1 \\ 1 & -1 \end{pmatrix} \ (52)$$

$$\boldsymbol{\alpha}_2 = \frac{1}{6\mathcal{R}}\begin{pmatrix} 1 & -1 \\ 1 & -1 \end{pmatrix} + \frac{4}{3}\frac{\beta}{\mathcal{R}}\begin{pmatrix} -2 & -1 \\ 1 & 2 \end{pmatrix} \ (53)$$

$$\boldsymbol{\alpha}_4 = \frac{11}{384}\frac{1}{\mathcal{R}}\begin{pmatrix}1 & -1\\ 1 & -1\end{pmatrix} + \frac{4}{9}\frac{\beta}{\mathcal{R}}\begin{pmatrix}2 & 1\\ -1 & -2\end{pmatrix} + \frac{8}{45}\frac{\beta^2}{\mathcal{R}}\begin{pmatrix}-8 & -7\\ 7 & 8\end{pmatrix} \quad (54)$$

At zeroth order, i.e. steady state, the solution is exactly matched with the Poiseuille flow solution, i.e. the inlet and outlet flows are equal to the driving pressure divided by the vessel resistance. The Poiseuille solution is thus the leading order term in the dynamic solution. The second order component of the solution (linearly proportional to frequency) then provides a dynamic 'correction' that is dependent upon the non-dimensional group defined by Equation 30. This term is in turn dependent upon both the vessel resistance and the compliance and hence dependent on both the fluid and vessel properties. Note that the inlet and outlet can be swapped round and the formulation will remain the same, as would be expected given the original equations. The fourth order component is proportional to the square of frequency and can be neglected to a high degree of accuracy (it is included here primarily for use in the following section).

As well as the frequency domain representation, it is useful to consider the results back in the time domain. Considering Equation 51 and truncating the solution after terms up to ε^2 gives:

$$\begin{pmatrix}q_{in}\\ q_{out}\end{pmatrix} = \boldsymbol{\alpha}_0\begin{pmatrix}p_{in}\\ p_{out}\end{pmatrix} - \frac{R^2}{\nu}\boldsymbol{\alpha}_2\frac{d}{dt}\begin{pmatrix}p_{in}\\ p_{out}\end{pmatrix} \quad (55)$$

These (first-order differential) equations can then be used to relate the flows and pressures in each vessel in a network, based on the two parameters β and $\mathcal{R}$, calculated for each vessel, by substituting in the expressions for $\boldsymbol{\alpha}_0$ and $\boldsymbol{\alpha}_2$ given in Equations 52 and 53 respectively. For example, in a single vessel, the inlet and outlet flows can be calculated directly from the inlet and outlet pressures using Equation 55 and specific values of the two parameters. For a single vessel, the model can be represented using two 2x2 matrices, relating the flows to the pressures; with the addition of each vessel to a network, an additional unknown variable will be added, increasing the size of the matrices by 1 in each dimension. This can then be done up to a network of arbitrary size, although it is likely that alternative mathematical formulations would be used in very large networks due to the computational cost.

For most networks this will be a sufficient representation, without the need for further terms: the first term on the left hand side of Equation 55 is the 'traditional' term that relates steady flow to a steady pressure difference along the vessel, with the second term adding in the dynamic effects that occur due to the oscillation of the fluid and the interaction between the unsteady fluid motion and an elastic wall. Note that the dynamic term thus exists even in a rigid vessel. We will consider in more detail how these equations can be linked together later, once we have considered the equations for volume and for connecting vessels in the next two sections, and then give an example of the solution obtained using this approach.

2.3 Result 3: Blood volume can be modelled as quasi-steady-state when $\omega T \ll 180$ (*ω* is driving frequency, *T* is vessel time constant)

In the previous result, we derived a relationship between the inlet and outlet flows and the driving pressures in a single vessel, Figure 1a. This enables us directly to consider changes in the volume of the vessel, *V*, through the difference between inlet and outlet flows:

$$\frac{dV}{dt} = q_{in} - q_{out} \quad (56)$$

In the frequency domain, using Equation 51 and Equation 56 gives:

$$i\omega\hat{V} = -4\frac{\beta}{\mathcal{R}}\varepsilon^2(1 \quad 1)\begin{pmatrix}\hat{p}_{in}\\ \hat{p}_{out}\end{pmatrix} + \varepsilon^4\frac{4}{9}\frac{\beta}{\mathcal{R}}\left(1-\frac{2}{5}\beta\right)(1 \quad -1)\begin{pmatrix}\hat{p}_{in}\\ \hat{p}_{out}\end{pmatrix} + \cdots \quad (57)$$

Substituting in Equation 28 and dividing by $i\omega$ (i.e. integrating) then gives:

$$\hat{V} = \frac{C}{2}(\hat{p}_{in} + \hat{p}_{out}) + i\omega\frac{R^2}{18\nu}\left(1-\frac{2}{5}\beta\right)C(\hat{p}_{in} - \hat{p}_{out}) + \cdots \quad (58)$$

Hence to first order, the volume is equal to the product of compliance with average pressure, as expected. The second term in Equation 58 is the dynamic component of volume changes: this is particularly important in the context of localised changes in flow in response to activation. This

second term can be considered to be a 'dynamic' compliance term. If we assume that β is large (strictly much larger than 5/2), then Equation 58 approximates to:

$$\hat{V} = \frac{C}{2}(\hat{p}_{in} + \hat{p}_{out}) - i\omega\frac{\beta R^2}{45\nu}C(\hat{p}_{in} - \hat{p}_{out}) + \cdots \quad (59)$$

We then formally define the product of resistance and compliance to be the time constant of the vessel:

$$T = \mathcal{R}C \quad (60)$$

and hence Equation 59 simplifies to (eliminating β using Equation 30):

$$\hat{V} = \frac{C}{2}\left[(\hat{p}_{in} + \hat{p}_{out}) - \frac{i\omega T}{180}(\hat{p}_{in} - \hat{p}_{out}) + \cdots\right] \quad (61)$$

Hence, the dynamic component can be neglected when $\omega T \ll 180$. Note that in the case where β is not much larger than 5/2, then the dynamic component in Equation 58 will depend primarily on the square of Womersley number, which then should be much less than 18 for the dynamic component to be negligible: since we have already discussed this in Section 2.3, we will not consider this case further. For completeness, as in the previous section, we convert Equation 61 back to the time domain:

$$V = \frac{C}{2}\left[(p_{in} + p_{out}) - \frac{T}{180}\frac{d}{dt}(p_{in} - p_{out}) + \cdots\right] \quad (62)$$

However, under the condition above ($\omega T \ll 180$), the volume then essentially follows a quasi-steady state dependence on the average pressure in the vessel as follows:

$$V = \frac{C}{2}(p_{in} + p_{out}) \quad (63)$$

Note of course that we have not considered the viscoelastic nature of the vessel wall, which would of course influence the result; however, the oscillation of the fluid makes only a negligible contribution to the effective compliance of the vessel under this condition.

2.4 Result 4: Matching of static pressure at nodes can be used when $\varepsilon Re_D \ll 100$ ($\boldsymbol{\varepsilon}$ is ratio of vessel radius to length, $\boldsymbol{Re_D}$ is Reynolds number based on vessel diameter)

In the previous two sections we have derived relationships for inlet and outlet flows and volume in a single vessel as a function of the inlet and outlet pressures. The final stage in modelling the cerebral vasculature is to connect the vessels together. The main consideration here is the choice of boundary conditions relating flows and pressures at the nodes that connect individual vessels. Once these have been determined, all of the flows and volumes can be determined.

The first boundary condition that is universally applied is conservation of flow at nodes, i.e. the flow entering a node and the flow exiting a node must balance at all times. However, there is less agreement over the second boundary condition, related to pressure; two approaches have been used, essentially assuming that either static pressure remains the same as flow passes from one vessel into the next (as the flow velocity changes, this means that energy is not conserved), or that total pressure (and hence energy) is conserved, as discussed in the Introduction. The former approach however has the advantage that it is a linear condition and thus results in less computationally expensive numerical solutions. We thus examine in this section whether or not there is a significant difference between the two approaches.

We consider a bifurcating node, as shown in Figure 1c, where a parent vessel supplies two child vessels, where the inlet and outlet to the parent vessel are termed nodes 1 and 2a respectively, and the inlet to both child vessels is termed node 2b, i.e. points 2a and 2b are taken to be immediately before and after the node. If we assume identical conditions in both child vessels, the velocities are in the ratio:

$$\frac{u_C}{u_P} = \frac{1}{2}\left(\frac{R_P}{R_C}\right)^2 \quad (64)$$

relative to that in the parent vessel, from conservation of flow, where the subscripts *P* and *C* refer to conditions in the parent and child vessels respectively. If we next assume Murray's law, Murray (1926), with exponent *n*, we can also calculate the ratio of the vessel radii:

$$(R_P)^n = (R_C)^n + (R_C)^n = 2(R_C)^n \quad (65)$$

since we are assuming identical child vessels. Hence:

$$\frac{u_C}{u_P} = \frac{1}{2}\left(2^{1/n}\right)^2 = 2^{\left(-1+\frac{2}{n}\right)} \quad (66)$$

Matching total pressure at the node gives:

$$p_{2a} + \frac{1}{2}\rho u_P^2 = p_{2b} + \frac{1}{2}\rho u_C^2 \quad (67)$$

We can thus calculate the change in pressure across the node, i.e. from the outlet of the parent vessel to the inlet of the child vessel, as a fraction of the inlet velocity head:

$$C_p = \frac{p_{2b} - p_{2a}}{\frac{1}{2}\rho u_P^2} = 1 - 2^{\frac{2(2-n)}{n}} \quad (68)$$

This is equal to 0 for *n* = 2, 0.18 for *n* = 7/3 and 0.37 for *n* = 3: these values being selected based on a number of studies that have examined the value of this exponent in a number of scenarios, see for example Mut et al. (2014). The largest value of this pressure coefficient is thus 0.37, which will tend to occur at the smallest length scales as this is where *n* is closest to 3. Note that it is of course also equal to 0 for the case of conservation of total pressure (the case where *n* = 2 is thus the only one where both are matched). Now compare this to the pressure loss due to friction in the parent vessel:

$$C_p = \frac{p_1 - p_{2a}}{\frac{1}{2}\rho u_P^2} = \frac{32}{\varepsilon Re_D} \quad (69)$$

where Reynolds number is here based on the parent vessel diameter, similar to Equation 4, and:

$$\varepsilon = \frac{R_P}{L_P} \quad (70)$$

is the radius to length ratio of the parent vessel (note that we again use ε in this section with a different definition from earlier). This calculation for head loss is based on the assumption of laminar flow (a reasonable approximation in this context since Reynolds number is low), as outlined in standard fluid mechanics texts, see for example Caro et al. (2012).

Since the largest head loss coefficient at a node (Equation 68) is equal to 0.37, as shown above, this is only comparable in magnitude to the head loss coefficient for an individual vessel (Equation 69) when the product εRe_D is approximately 100. Hence, if this product is less than 100, the difference between assuming matched static pressure and matched total pressure is small, since the head loss across the node is small in comparison with the head loss along the upstream vessel. Since the matching of static pressure results in linear equations, this can be used under this condition to simplify the solution procedure without significant loss of accuracy. The question of whether static or total pressure should be matched in the vessels where this condition does not hold is a difficult one and one that needs further investigation but which is outside the scope of this paper.

2.5 Result 5: Flow in a network can be solved using a series of matrices

Based on Result 4, we can assume matched static pressure at nodes without any significant loss of accuracy if $\varepsilon Re_D < 100$. The resulting equations for a network, for example that shown in Figure 1d, can then be expressed in matrix form:

$$\boldsymbol{\alpha}_{int}\mathbf{p}_{int} = \boldsymbol{\alpha}_{ext}\mathbf{p}_{ext} \quad (71)$$

in terms of the (unknown) pressures at the internal nodes and the (known) pressures at the external nodes. Equation 71 holds separately for each order of the solution. Once the matrices have been formulated, Equation 71 can be solved for the unknown internal node pressures separately for each order and the flows calculated through each vessel using the formulation above. Note that this can

be done in either the time domain or the frequency domain; in the latter case, it should be noted that our approach, through exploitation of small values of Womersley number, is considerably simpler than the method of Flores et al. (2016). The approach can of course be applied to networks of arbitrary complexity as long as the assumptions are valid in every vessel, although for very large networks it would be more likely that alternative methods (such as homogenisation techniques) would be applied, see for example the approach proposed by El-Bouri and Payne (2015).

3 Numerical simulations

Having completed this analysis, we now consider the results in the context of previous models. In particular we directly consider those models that model dynamic changes in the flow field. These models, Boas et al. (2008), Reichold et al. (2009), Gagnon et al. (2015) and Payne and Lucas (2017), are actually very similar in their approach, using a non-linear compliance model coupled with the Poiseuille equation that uses an empirical model for viscosity based on vessel diameter and haematocrit (which is taken to vary with vessel diameter). Although we have assumed a constant compliance in our analysis here, we have shown that the assumption of quasi steady state (inherent in all of the models listed above) is a valid one over all of the length scales that occur within the cerebral vasculature.

However, we have shown in our analysis how to model the dynamic relationship between flow and pressure in individual vessels and this has not been considered by the models listed above, where only the leading order (Poiseuille) term is considered. Although the result given in Equation 55 is more complicated, the dynamic term is not negligible in time-varying flow fields. We will illustrate the effect that this can have in the simulations that we present below.

We consider the very simple bifurcating network shown in Figure 2 below, where we take the vessel properties from the model proposed by Payne and Lucas (2017), as given in Table 2. We use this network model as it is very similar to that proposed by Boas et al. (2008), where different modelling

assumptions were applied, as we will discuss below. It thus provides a simple means of comparison of the dynamic behaviour of the model.

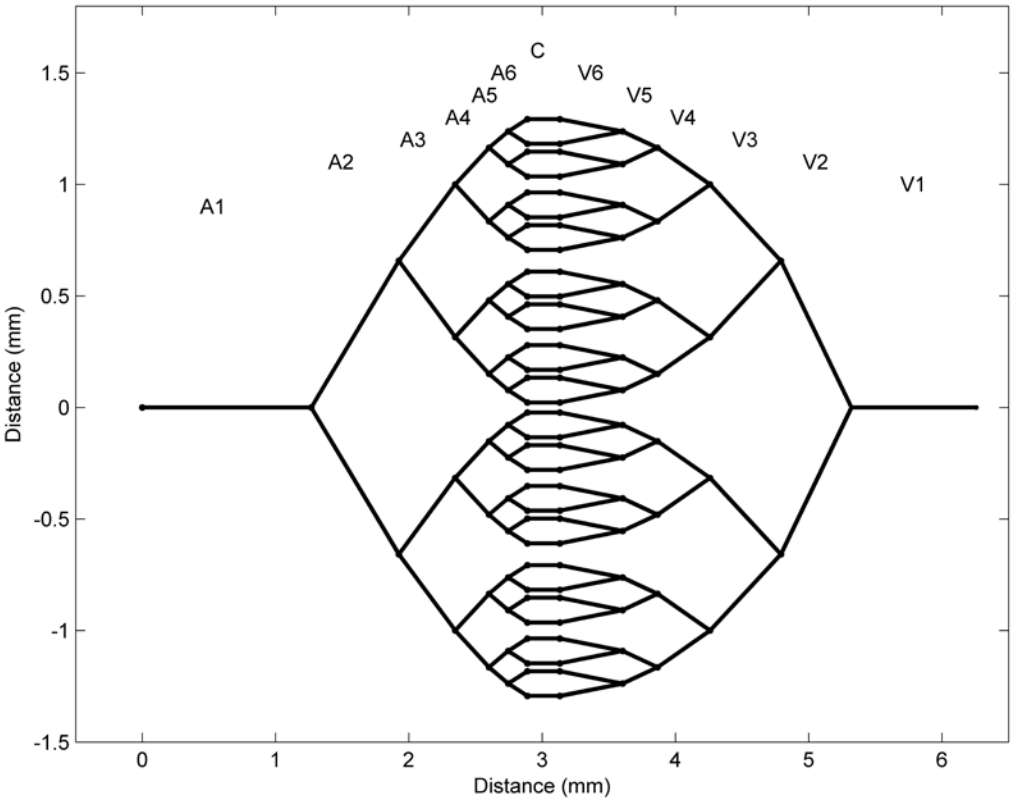

Figure 2 Bifurcating network used in model simulations

Branch	Number of vessels	Diameter	Length	Wall thickness	Velocity	Viscosity	Pressure drop	Saturation
		µm	µm	µm	mm/s	mPa.s	mmHg	%
A1	1	23.97	1267.6	4.84	8.2	1.59	6.93	94
A2	2	19.17	930.3	4.25	6.41	1.50	5.87	93
A3	4	15.28	543.6	3.81	5.05	1.42	4.02	92
A4	8	12.08	302.3	3.49	4.03	1.34	2.70	89
A5	16	9.46	161.2	3.27	3.29	1.28	1.82	84

A6	32	7.32	154.7	3.14	2.75	1.23	2.35	76.5
C	64	8	243.9	0.309	2.30	1.24	2.62	66.5
V6	32	11.51	473.9	1.15	1.11	1.33	1.27	61
V5	16	14.53	272.3	1.45	1.40	1.40	0.61	59.75
V4	8	17.79	426.6	1.78	1.86	1.48	0.89	58.75
V3	4	21.45	632.5	2.15	2.56	1.55	1.31	58.25
V2	2	25.70	844.2	2.57	3.57	1.62	1.78	57.75
V1	1	30.77	936.3	3.08	4.97	1.70	2.01	57.25

Table 2 Vascular parameters used in network model

For comparison, we plot the results obtained for the same network but using the flow and volume model proposed by Boas et al. (2008) and used by other authors; the equations in this and in our model are set out for comparison and for convenience of reference in Table 3. This approach assumes that there is an instantaneous equilibrium between flow and pressure:

$$q_{ij} = \frac{1}{\mathcal{R}_{ij}}\left(p_i - p_j\right) \quad (72)$$

between nodes *i* and *j*, i.e. as Equation 55, but neglecting all dynamic terms. It then assumes that the volume of each vessel, V_i, follows changes in pressure through a non-linear relationship of the form:

$$p_i - p_{ic} = kV_i^{\beta} \quad (73)$$

where *k* is a constant, set by baseline conditions, and β is a compliance parameter that is set to 2 by Boas et al. (2008). The loop of equations is closed by conservation of volume:

$$\frac{dV_i}{dt} = q_{i,in} - q_{i,out} \quad (74)$$

These equations can easily be solved dynamically for the same dynamic inlet pressure and network parameters given above.

	New approach	Previous approach
Pressure-flow relationship	$\begin{pmatrix} q_{in} \\ q_{out} \end{pmatrix} = \boldsymbol{\alpha}_0 \begin{pmatrix} p_{in} \\ p_{out} \end{pmatrix} - \frac{R^2}{\nu} \boldsymbol{\alpha}_2 \frac{d}{dt} \begin{pmatrix} p_{in} \\ p_{out} \end{pmatrix}$ (Equation 55)	$q_{ij} = \frac{1}{\mathcal{R}_{ij}} (p_i - p_j)$ (Equation 72)
Pressure-volume relationship	$V = \frac{C}{2} (p_{in} + p_{out})$ (Equation 63)	$p_i - p_{ic} = k V_i^{\beta}$ (Equation 73)
Flow-volume relationship	$\frac{dV}{dt} = q_{in} - q_{out}$ (Equation 56)	$\frac{dV_i}{dt} = q_{i,in} - q_{i,out}$ (Equation 74)
Nodal relationship	Conservation of flow Matching of static pressure	Conservation of flow Matching of static pressure

Table 3 Summary of model equations in both approaches; for terminology, see original equations

We now illustrate our approach by considering the response to changes in inlet pressure. For simplicity, we assume a reduction in inlet pressure from 60 mmHg to 48 mmHg (a drop of 20 %). In order to give a smoothly varying inlet pressure, we assume a function of the form:

$$p_{in} = P_a \left[1 + \left(\frac{k-1}{2} \right) \left(1 + \tanh \left(\frac{t-1}{0.1} \right) \right) \right] \quad (75)$$

with *k* denoting the fractional value of baseline pressure to which the function tends, set here to 0.8 (i.e. a 20 % drop in driving pressure). This drop occurs at a time of 1 second (allowing the model to settle before the change occurs) with a rapid rate of change. The resulting changes in nodal pressure and vessel volume across all 13 generations are then calculated using both sets of model equations set out in Table 4.

We first examine the changes in blood pressure within the network. Since our new approach is based on nodal pressures and the previous approach on pressures in the middle of the vessel, we interpolate the nodal pressures to plot the pressures half way along the vessels. We plot the pressures in the third generation of the arteriolar bed, in the capillary bed, and in the fourth

generation of the venous bed for both models, as shown in Figure 3. We assume a value of 10 mmHg for intracranial pressure and an exponent of 1 in Equation 73; we then calculate the value of *k* from baseline conditions.

It is clear from Figure 3 that the changes in pressure propagate downstream from inlet to outlet, with the largest and fastest changes occurring at the vessels closest to the inlet. Whilst the response times to changes in inlet blood pressure in these vessels is of order only a couple of seconds, as shown in Figure 3, we note that the response is not instantaneous, and care thus needs to be taken in calculating the flow response to changes in inlet pressure since there is a delay in the propagation of pressure changes through the network. Without considering the delay, there would be an instantaneous response in all vessels.

The previous model exhibits a much faster response throughout the vasculature; this is caused by neglecting the second term in Equation 55. As a result, the speed of response is substantially different; our model shows how the dynamic term in Equation 55 does play an important role in setting the speed of response, even at this small length scale. Estimating the time constant of the response yields values of 0.17, 0.76 and 1.15 seconds in our new model for the mid-arteriolar, capillary and mid-venous vessels respectively, compared to 0.14, 0.34 and 0.47 seconds for the previous model, showing how although the earlier vessels respond at a similar speed, the later vessels respond much more slowly.

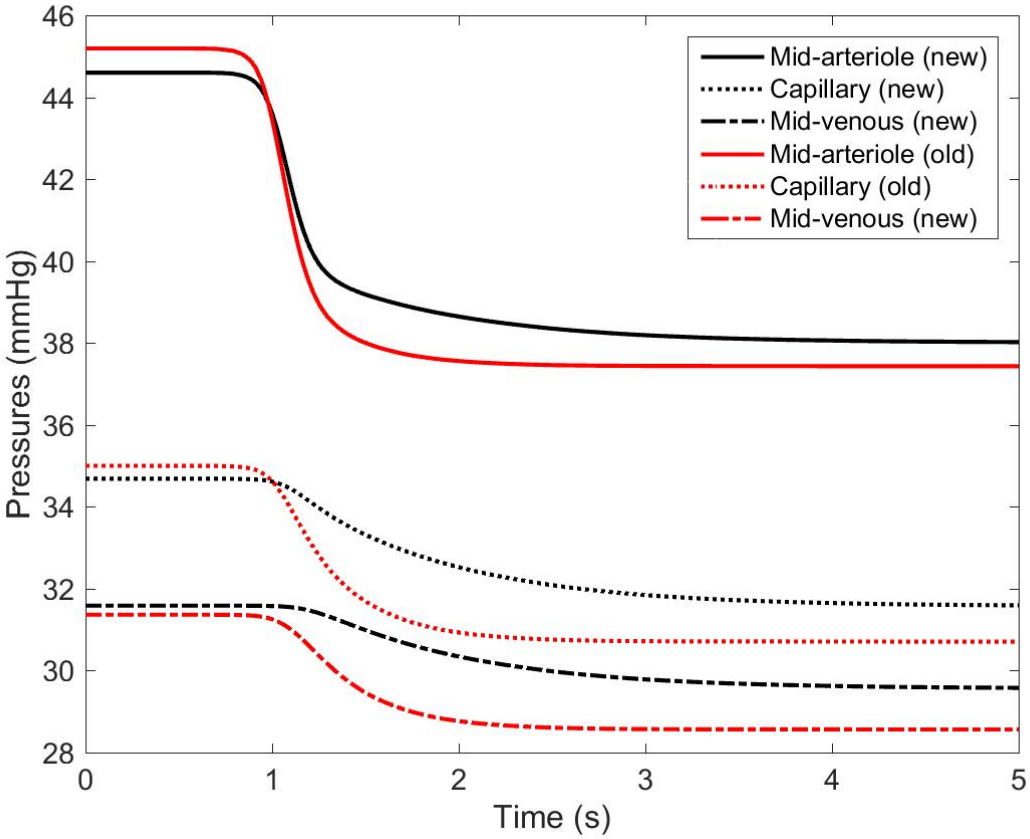

Figure 3 Dynamic changes in blood pressures in bifurcating network in response to 20 % decrease in inlet blood pressure (for definitions of locations, see main text)

The results for volume, Figure 4, follow those for pressure, as would be expected from the analysis above and the justification of quasi steady state behaviour in response to changes in pressure. The later generations of the network thus respond much more slowly in response to changes in inlet blood pressure than would be assumed from the previous modelling approach. This difference is caused by the fact that previous approaches assumed a dynamically varying volume in response to instantaneous changes in pressure: our analysis shows rather that pressure responds dynamically to changes in inlet conditions with volume following these pressure changes quasi-statically (and hence with the same delay as the pressure changes).

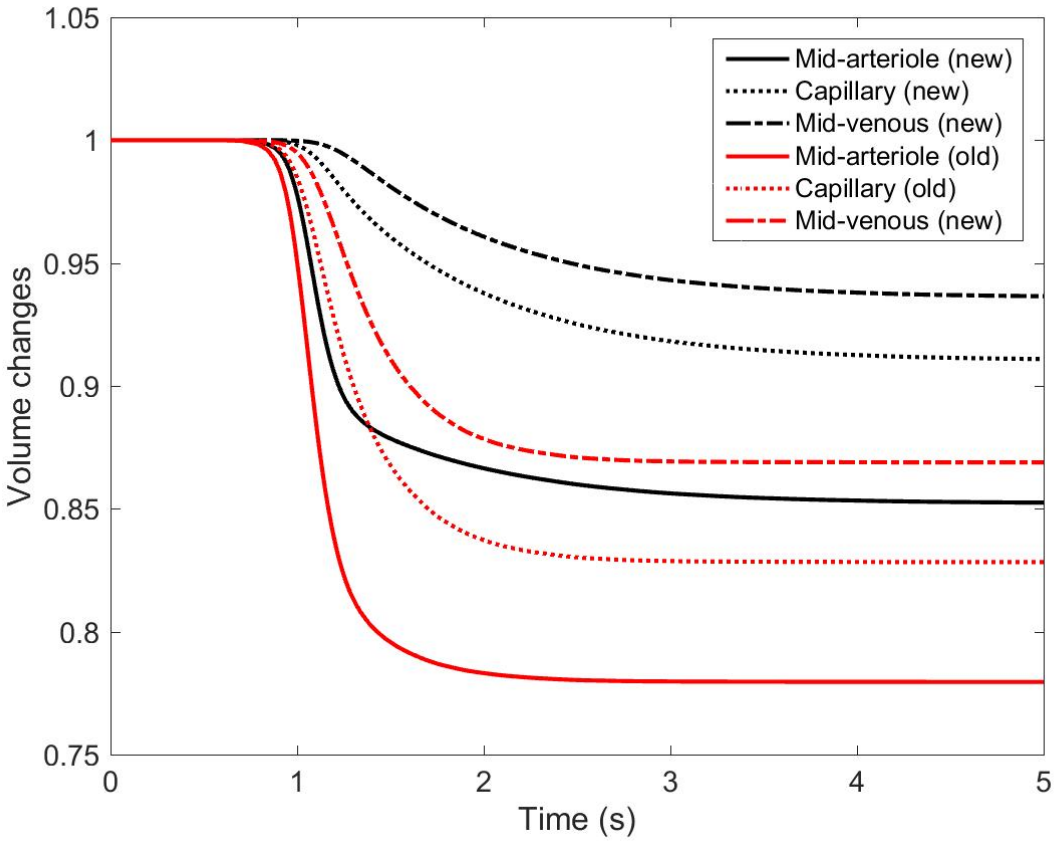

Figure 4 Dynamic changes in blood volumes in bifurcating network in bifurcating network in response to 20 % decrease in inlet blood pressure (for definitions of locations, see main text)

This is an important distinction and the fact that the changes in pressure and volume have now been shown to be slower than previously thought will significantly alter the dynamic behaviour of pressure and volume changes in models of the cerebral microvasculature. Note that the differences in absolute values of volumes between the two models, shown in Figure 4, are due to the slightly different models that are used for compliance in the two approaches; however this does not affect the main finding of this study. Experimental validation, through simultaneous measurements of blood flow and blood volume will be extremely valuable in validating the approach set out here and quantifying the importance of the dynamic term in Equation 55.

4 Discussion

In the previous section we have shown that the non-linear advection term can be neglected, when considering both single vessels and the flow field as a continuum; derived a relationship between inlet and outlet flows in single vessels and inlet and outlet pressures; derived the condition for a quasi-steady-state approximation for blood volume; and then shown how single vessels can be linked together and the flow field in a network solved as a matrix problem. For each of these derivations there is a limit on the validity of the approximation: we thus consider these now in the particular context of the cerebral vasculature. We will then also consider the limitations of the approach that we have adopted. We should note that since we are basing many of the assumptions on order of magnitude arguments, the precise values are often less important than the relative magnitudes of different parameters.

We will assume throughout this section that blood has a density of 1040 kg/m^3 and a kinematic viscosity of approximately 3 µPa.s (we will consider the value of viscosity in more detail below) and that the oscillation frequency is approximately 1 Hz (based on a typical heart rate of around 60 beats per minute), see for example Caro et al. (2012). We can therefore quantify the magnitude of the Womersley number immediately. This has magnitude less than one in vessels smaller than approximately 1.4 mm in diameter. The first order model presented in Result 2 is thus only valid for vessels of such diameter. Since the lower limit for imaging individual vessels is down to those with diameters of approximately 0.8-0.9 mm, see for example Mut et al. (2014), this approach does thus cover all of the generations of 'unseen' vessels and can therefore be applied to these vessels, i.e. those of diameter less than approximately 1.4 mm.

We next consider the product ωT. As a first approximation, we assume the same elastic isotropic model of the vessel wall as in Section 2.1; this then yields, see for example Chappell and Payne (2016):

$$\omega T = 12\left(\frac{\mu\omega}{E}\right)\left(\frac{L^2}{Rh}\right) \quad (76)$$

where the right hand side comprises non-dimensional groups, as shown in brackets, the latter based on the geometry of the vessel and the former based on a mixture of properties. If we assume a value of wall Young's modulus of 10^4 Pa, Caro et al. (2012), then this former term is approximately equal to 2×10^{-6}. The condition for the quasi-steady-state volume relationship then becomes approximately $Rh/L^2 > 1.2\text{x}10^{-7}$, which is satisfied by every vessel in the cerebral vasculature, since the radius to length ratio is rarely less than 0.01 and the wall thickness to radius ratio is normally in the range 0.1 to 0.5, see for example Payne (2007), Lucas (2012), Caro et al. (2012) and Payne (2017). It is worth noting that this is in good agreement with recent studies into the neurovascular coupling response, which have indicated a relatively small volume component to the short term response, Hillman et al. (2007), Vazquez et al. (2010) and Drew et al. (2011). It also points away from the use of the delayed compliance model, Kong et al. (2004) and Zheng and Mayhew (2009), since the time constant has been shown here to be negligible in all vessels in the cerebral vasculature.

We next consider the ratio $\frac{E}{\rho U^2}\frac{h}{R}$, which needs to be much greater than 3/2 for advection to be neglected. Since the ratio of wall thickness to radius, $\frac{h}{R}$, is typically in the range 0.1 to 0.5 (see above) in any vessel, a lower bound for this can be taken to be 0.1: the ratio $\frac{E}{\rho U^2}$ needs to be much greater than approximately 15. The flow velocity thus needs to be much less than $\sqrt{E/15\rho}$, which, for the values of wall Young's modulus and blood density quoted above, is equivalent to being much less than approximately 0.8 m/s. This is well above any flow velocity found in the cerebral vasculature under normal conditions, Lucas (2012) and Payne (2017), and thus advection terms can be neglected throughout the cerebral vasculature, although it should be noted that under certain conditions, for example severe stenosis, flow velocities can rise substantially and that care would have to be taken under such circumstances to re-evaluate this approximation.

Finally, we consider the product εRe_D, which should be below 100 for the difference between matching of static and total pressures to be negligible. In the largest blood vessels in the brain, the

flow velocity is of order 0.5 m/s with diameters of order 5 mm, see for example Lucas (2012). Such values give a Reynolds number based on diameter of approximately 1000. Since the typical radius to length ratio values found in these large vessels are of order 0.1, Mut et al. (2014), the product εRe_D is thus of order 100 in the largest vessels in the brain. The difference between matched static and matched total pressure can thus be significant in these largest vessels; however, in the vessels below the imaging threshold of approximately 1 mm in diameter, Mut et al. (2014), this ratio will be below this limit, making the matching of static pressure a justifiable assumption in such vessels. Care simply needs to be taken when modelling the larger vessels, essentially those that can be imaged directly. In these vessels, the product εRe_D can be calculated for each vessel and the assumption of matched static pressure examined in each individual vessel.

We have thus explored how the four relationships derived earlier relate to individual blood vessels in the cerebral vasculature. It has been shown that advection can always be neglected in the equation governing blood flow and that blood volume can be assumed to be in quasi-steady state at all times; however, the first order approach for pressure and flow (arising from the perturbation series analysis) and the matching of static pressure should only be applied in vessels below approximately 1 mm in diameter (using this as an approximate threshold for the distinction). Since this approximately corresponds to the imaging threshold, it is then possible to apply all four simplifications to models at this length scale. This does make the application of such models significantly easier. For simplicity we summarise these results in Table 4 below.

	Vessels of diameter < 1 mm	**Vessel of diameter > 1 mm**
Neglect advection	Yes	Yes
First order model	Yes	No
Blood volume quasi steady state	Yes	Yes
Match static pressure	Yes	Possibly

Table 4 List of assumptions in vessels of different diameter

Note that whilst we have considered every vessel in each generation to respond in exactly the same manner, due to the symmetry of the change that we have imposed (and for simplicity of presentation), it would easily be possible to consider the response to localised changes in individual vessels, as has been examined by other authors; although it should be noted that this model is at present a purely passive one and that a model of the active response should be coupled with this model in future to provide good agreement with experimental data, for example examining the response to activation, as discussed in the Introduction.

It would be possible to characterise the overall behaviour of the network in terms of lumped values of resistance and compliance, reducing the network to simpler form: characterising the response of the network to changes in terms of time constants would be a valuable exercise, since this enables the behaviour of the network to be considered as a whole, along the lines of the 6 second time constant for oxygen transport in the same network found by Payne and Lucas (2017). This would help to construct more detailed models of the larger vasculature, of which this network is only one very small part. However, the approach set out in Table 3 under the restrictions set out in Table 4 can be used across the cerebral vasculature and it is suggested that these modelling equations, validated by the analysis presented earlier, be used in this context in place of the other approaches that have been used.

It is worth noting that alongside the model framework presented here that considers each vessel individually, we also discussed earlier the use of a continuous approach to flow in the microvasculature, based on the work of El-Bouri and Payne (2015) in providing a Darcy approximation for the capillary flow field, as presented above, that has been coupled to a network model in El-Bouri and Payne (2018), as shown in Figure 1d. This approach offers a complementary method to the ‘discrete’ flow field presented here, since the two approaches can be coupled together, dependent upon the length scale being considered and the size of the network that is

being studied, potentially reducing the computation time very significantly by exploiting the wide range of length scales.

We do note that there are a number of limitations to the analysis above. We have assumed axisymmetric vessels and flow fields, which is a reasonable assumption to these flows, although care should be taken when considering vessels with any significant tortuosity. A more significant assumption, however, is that we have assumed the fluid to be Newtonian, which does limit the analysis. However, since the non-Newtonian effects will be greatest in the smaller vessels, which we have found to be furthest away from the limits derived here, it thus seems reasonable to assume that the non-Newtonian effects will have little impact on the results found here, although a more rigorous analysis would be required to justify this more completely.

We have also neglected variations in haematocrit, which can have a significant impact on the flow field throughout microvascular networks, Gould and Linninger (2015). The choice of model for haematocrit distribution can also strongly influence the local flow patterns, although further examination of the effects of this on the overall network behaviour is still needed. It would be extremely interesting to examine the effects of the variability in haematocrit distribution on the results that we have presented here.

In addition to this, future work will also involve extending the analysis to the transport of oxygen and glucose between blood and tissue, using the approach set out in Payne and Lucas (2017), since solving these equations is key to understanding the relationship between flow and metabolism. The coupled nature of the equations means that this is a more difficult problem to investigate, although considerable progress has been made by many of the studies listed in the Introduction. However, by doing so, it will be possible to develop more rigorous models of both flow and metabolism that will hopefully help to provide more insight into their behaviour in both normal and abnormal physiological conditions.

This will also help to link to models of the BOLD response, providing a sounder theoretical justification for the haemodynamic components of such models, in particular the lumped parameter components, which often have to be assumed on a somewhat ad hoc basis, see for example Aquino et al. (2014). Such multi-scale modelling approaches have a great deal to offer in terms of understanding the relationship between the underlying physiology and experimental measurements and provide a rich avenue for exploration in the future. They also offer the possibility of experimental validation through the characterisation of models over different length scales, enabling the assumptions used in the model proposed here to be more directly tested, using potentially a very wide range of measurement modalities, including but not restricted to BOLD, MRI and PET.

Appendix A

A fundamental assumption when using homogenization is that the large-scale structure, in this case the capillary bed, is locally periodic. This allows the removal of secular terms in multi-dimensional problems without the need to solve higher order equations explicitly. It is of course possible to homogenize non-locally periodic structures, however finding the solvability condition to eliminate the secular terms becomes very difficult. Periodicity is thus regularly used in homogenization to simplify the removal of secular terms and is used here.

As $\varepsilon \ll 1$ the local and macro length scales are well-separated and can be defined as $\mathbf{X}$ and $\mathbf{x} = \varepsilon\mathbf{X}$ respectively. Using the assumption of scale separation both $\mathbf{x}$ and $\mathbf{X}$ can be treated as independent variables and so

$$\nabla = \nabla_X + \varepsilon\nabla_x, \qquad \nabla^2 = \nabla_X^2 + 2\varepsilon\nabla_x.\nabla_X + \varepsilon^2\nabla_x^2 \quad (\mathrm{A.1})$$

Using this to expand out Equation 17 gives:

$$\varepsilon^2 Re_D[(\mathbf{u}_c.\nabla_{\boldsymbol{X}})\mathbf{u}_c + \varepsilon(\mathbf{u}_c.\nabla_{\boldsymbol{x}})\mathbf{u}_c] = -\nabla_{\boldsymbol{X}}p_c - \varepsilon\nabla_{\boldsymbol{x}}p_c + \varepsilon\nabla_{\boldsymbol{X}}^2\mathbf{u}_c + 2\varepsilon^2\nabla_{\boldsymbol{x}}.\nabla_{\boldsymbol{X}}\mathbf{u}_c + \varepsilon^3\nabla_x^2\mathbf{u}_c \quad \text{in } \Omega_c \quad (\mathrm{A.2})$$

We also use non-dimensional forms of the continuity equation and the boundary conditions:

$$\nabla_{\boldsymbol{X}}.\mathbf{u}_c + \varepsilon\nabla_{\boldsymbol{x}}.\mathbf{u}_c = 0 \quad \text{in } \Omega_c \quad (\mathrm{A.3})$$

$$\mathbf{u}_c.\boldsymbol{n} = 0 \quad \text{on } \Gamma_c \quad (\mathrm{A.4})$$

$$\mathbf{u}_c.\boldsymbol{\tau} = 0 \quad \text{on } \Gamma_c \quad (\mathrm{A.5})$$

where Ω_c denotes the blood space and Γ_c denotes the boundary between blood and tissue. We then apply the multiple scales expansion for velocity and pressure given in Equations 20 and 21. In order to maintain periodicity each component of $\mathbf{u}$ and p is assumed to be periodic in $\mathbf{X}$. The expansions of Equations 20 and 21 are substituted into Equations A.2-A.5 and successive orders of ε equated to determine the leading order homogenized equations for capillary flow and pressure:

$$\varepsilon^2 Re_D[((\mathbf{u}_c^{(0)} + \varepsilon\mathbf{u}_c^{(1)} + \cdots).\nabla_{\boldsymbol{X}})(\mathbf{u}_c^{(0)} + \varepsilon\mathbf{u}_c^{(1)} + \cdots) + \varepsilon((\mathbf{u}_c^{(0)} + \varepsilon\mathbf{u}_c^{(1)} + \cdots).\nabla_{\boldsymbol{x}})(\mathbf{u}_c^{(0)} + \varepsilon\mathbf{u}_c^{(1)} + \cdots)] = -\nabla_{\boldsymbol{X}}\,(p_c^{(0)} + \varepsilon p_c^{(1)} + \cdots) - \varepsilon\nabla_{\boldsymbol{x}}(p_c^{(0)} + \varepsilon p_c^{(1)} + \cdots) + \varepsilon\nabla_{\boldsymbol{X}}^2(\mathbf{u}_c^{(0)} + \varepsilon\mathbf{u}_c^{(1)} + \cdots) + 2\varepsilon^2\nabla_{\boldsymbol{x}}.\nabla_{\boldsymbol{X}}\left(\mathbf{u}_c^{(0)} + \varepsilon\mathbf{u}_c^{(1)} + \cdots\right) + \varepsilon^3\nabla_{\boldsymbol{x}}^2\left(\mathbf{u}_c^{(0)} + \varepsilon\mathbf{u}_c^{(1)} + \cdots\right) \text{ in } \Omega_c \quad (\text{A. 6})$$

$$\nabla_{\boldsymbol{X}}.\left(\mathbf{u}_c^{(0)} + \varepsilon\mathbf{u}_c^{(1)} + \cdots\right) + \varepsilon\nabla_{\boldsymbol{x}}.\left(\mathbf{u}_c^{(0)} + \varepsilon\mathbf{u}_c^{(1)} + \cdots\right) = 0 \quad \text{in } \Omega_c \quad (\text{A. 7})$$

$$\left(\mathbf{u}_c^{(0)} + \varepsilon\mathbf{u}_c^{(1)} + \cdots\right).\boldsymbol{\tau} = 0 \quad (\text{A. 8})$$

$$\left(\mathbf{u}_c^{(0)} + \varepsilon\mathbf{u}_c^{(1)} + \cdots\right).\boldsymbol{n} = 0 \quad (\text{A. 9})$$

Equating powers of $O(\varepsilon^0)$ in Equations A.6-A.9 gives:

$$\nabla_{\boldsymbol{X}}\, p_c^{(0)} = 0 \quad (\text{A. 10})$$

$$\nabla_{\boldsymbol{X}}.\,\mathbf{u}_c^{(0)} = 0 \quad (\text{A. 11})$$

$$\mathbf{u}_c^{(0)}.\boldsymbol{\tau} = 0 \text{ and } \mathbf{u}_c^{(0)}.\boldsymbol{n} = 0 \quad \text{on } \Gamma \quad (\text{A. 12})$$

and equating powers of $O(\varepsilon^1)$:

$$\nabla_{\boldsymbol{X}}\, p_c^{(1)} + \nabla_{\boldsymbol{x}} p_c^{(0)} = \nabla_{\boldsymbol{X}}^2\mathbf{u}_c^{(0)} \quad (\text{A. 13})$$

$$\nabla_{\boldsymbol{X}}.\,\mathbf{u}_c^{(1)} + \nabla_{\boldsymbol{x}}.\,\mathbf{u}_c^{(0)} = 0 \quad (\text{A. 14})$$

$$\mathbf{u}_c^{(1)}.\boldsymbol{\tau} = 0 \text{ and } \mathbf{u}_c^{(1)}.\boldsymbol{n} = 0 \quad \text{on } \Gamma \quad (\text{A. 15})$$

From Equation A.10 it is evident that $p_c^{(0)}$ is constant at the local-scale, hence $p_c^{(0)} = p_c^{(0)}(\mathbf{x})$. In order to determine the leading order problem it is necessary to solve for $\mathbf{u}_c^{(0)}$and $p_c^{(1)}$. From Equation A.13 it can be seen that $\mathbf{u}_c^{(0)}$ and $p_c^{(1)}$ are both linear functions of $\nabla_{\boldsymbol{x}} p_c^{(0)}$ and so solutions are proposed of the form:

$$\mathbf{u}_c^{(0)} = -\boldsymbol{w}_c^j(\mathbf{X})\frac{dp_c^{(0)}}{dx^j} \quad (\text{A. 16})$$

$$p_c^{(1)} = -P_c^j(\mathbf{X})\frac{dp_c^{(0)}}{dx^j} + \bar{p_c}^{(1)} \quad (\text{A. 17})$$

Einstein notation has been used here for clarity where j can take the values 1, 2, or 3 and refers to the Cartesian co-ordinate directions. The notation used is a simple substitution for what would otherwise be a dot product of the two j components. $\boldsymbol{w}_c^j(\mathbf{X})$ and $P_c^j(\mathbf{X})$ account for the local variations in $\mathbf{u}_c^{(0)}$ and $p_c^{(1)}$ and are known as the cell variables. It is from these local variables that the homogenized macro-scale parameters of the blood flow in the capillary network can be determined. These variables are determined by inserting them into Equations A.10-A.12 to obtain the cell problem:

$$\nabla_{\mathbf{X}}.\boldsymbol{w}_c^j(\mathbf{X}) = 0 \quad \text{in } \Omega_c \text{ (A.18)}$$

$$\nabla_{\mathbf{X}} P_c^j(\mathbf{X}) = \nabla_{\mathbf{X}}^2 \boldsymbol{w}_c^j(\mathbf{X}) + \mathbf{e}_j \quad \text{in } \Omega_c \text{ (A.19)}$$

$$\boldsymbol{w}_c^j(\mathbf{X}).\boldsymbol{\tau} = 0 \text{ and } \boldsymbol{w}_c^j(\mathbf{X}).\boldsymbol{n} = 0 \quad \text{on } \Gamma \text{ (A.20)}$$

where $\mathbf{e}_j$ is the unit vector in the j-direction. This is the local periodic cell problem which must be solved numerically in order, as shall be seen, to derive the parameters for the macro-scale problem. Note that Equation A.19 is a forced Stokes flow problem. From this is derived the Poiseuille equation (making assumptions on the radial and swirl components of the velocity). Therefore, despite having left in the convective acceleration term in the original equations, to leading order the cell problem is Stokes flow.

From Equations A.19-A.20 it can be seen that the cell problem is underdetermined and hence the local pressure term P_c^j is only defined up to a constant value. A uniqueness condition is thus imposed which states that the volume average of the local pressure is zero:

$$\langle P_c^j \rangle_c = \frac{1}{|\Omega|} \int_{\Omega_c} P_c^j \, dV = 0 \text{ (A.21)}$$

Taking a volume average over $\mathbf{u}_c^{(0)}$, Equation A.16 results in:

$$\langle \mathbf{u}_c^{(0)} \rangle_{\Omega_c} = -\mathbf{K} \nabla_x p_c^{(0)} \text{ (A.22)}$$

where

$$K_{ij} = \frac{1}{|\Omega|} \int_{\Omega_c} w_{ci}^j \, dV \text{ (A.23)}$$

This is Darcy's Law with $\mathbf{K}$ defining the permeability tensor. Therefore, to leading order, the homogenization of the incompressible, steady state Navier-Stokes equations gives Darcy's Law. The permeability tensor $\mathbf{K}$ encapsulates the geometry of the problem and how the geometry affects the flow for given pressure gradients. It is an averaged coefficient tensor, calculated by solving the micro cell problem, and is the volume average of the velocities in the cell problem.

References

Abramowitz M, Stegun I. Handbook of Mathematical Functions. United States Department of Commerce, National Bureau of Standards. 1964.

Acheson DJ. Elementary Fluid Dynamics. Oxford University Press. 1990.

Alastruey J, Parker KH, Peiró J, Byrd SM, Sherwin SJ. Modelling the circle of Willis to assess the effects of anatomical variations and occlusions on cerebral flows. J Biomech. 2007;40(8):1794-805.

Aquino KM, Robinson PA, Drysdale PM. Spatiotemporal hemodynamic response functions derived from physiology. J Theor Biol. 2014 Apr 21;347:118-36. doi: 10.1016/j.jtbi.2013.12.027. Epub 2014 Jan 4.

Aquino KM, Robinson PA, Schira MM, Breakspear M. Deconvolution of neural dynamics from fMRI data using a spatiotemporal hemodynamic response function. Neuroimage. 2014 Jul 1;94:203-215. doi: 10.1016/j.neuroimage.2014.03.001. Epub 2014 Mar 12.

Blinder P, Shih AY, Rafie C, Kleinfeld D. Topological basis for the robust distribution of blood to rodent neocortex. Proc Natl Acad Sci USA. 2010;107:12670–12675.

Boas DA, Jones SR, Devor A, Huppert TJ, Dale AM. A vascular anatomical network model of the spatio-temporal response to brain activation. Neuroimage. 2008 Apr 15;40(3):1116-29.

Buxton RB, Wong EC, Frank LR. Dynamics of blood flow and oxygenation changes during brain activation: the balloon model. Magn Reson Med. 1998 Jun;39(6):855-64.

Canic S, Kim EH. Mathematical analysis of the quasilinear effects in a hyperbolic model of blood flow through compliant axi-symmetric vessels. Math. Meth. Appl. Sci. 2003; 26: 1161–1186.

Caro CG, Pedley TJ, Schroter RC and Seed WA. The mechanics of the circulation, 2nd edition. Cambridge University Press, 2012.

Cassot F, Lauwers F, Fouard C, Prohaska S, Lauwers-Cances V. A novel three-dimensional computer-assisted method for a quantitative study of microvascular networks of the human cerebral cortex. Microcirculation. 2006 Jan;13(1):1-18.

Chappell MA, Payne SJ. Physiology for Engineers. Springer. 2016.

Drew PJ, Shih AY, Kleinfeld D. Fluctuating and sensory-induced vasodynamics in rodent cortex extend arteriole capacity. Proc Natl Acad Sci U S A. 2011 May 17;108(20):8473-8. doi: 10.1073/pnas.1100428108.

Duvernoy HM, Delon S, Vannson JL. Cortical blood vessels of the human brain. Brain Res Bull. 1981 Nov;7(5):519-79.

El-Bouri WK. Multi-scale modelling of the microvasculature in the human cerebral cortex. DPhil thesis, University of Oxford, 2017.

El-Bouri WK, Payne SJ. Multi-scale homogenization of blood flow in 3-dimensional human cerebral microvascular networks. J Theor Biol. 2015 Sep 7;380:40-7.

El-Bouri WK, Payne SJ. A statistical model of the penetrating arterioles and venules in the human cerebral cortex. Microcirculation. 2016 Oct;23(7):580-590. doi: 10.1111/micc.12318.

El-Bouri WK, Payne SJ. Investigating the effects of a penetrating vessel occlusion with a multi-scale microvasculature model of the human cerebral cortex. Neuroimage. 2018 Jan 28;172:94-106. doi: 10.1016/j.neuroimage.2018.01.049.

Fang Q, Sakadzic S, Ruvinskaya L, Devor A, Dale AM, Boas DA. Oxygen advection and diffusion in a three- dimensional vascular anatomical network. Optics Express. 2008;16:17530–17541.

Flores J, Alastruey J, Corvera Poiré E. A Novel Analytical Approach to Pulsatile Blood Flow in the Arterial Network. Ann Biomed Eng. 2016 May 2.

Formaggia L, Nobile F, Quarteroni A and Veneziani A. Multiscale modelling of the circulatory system: a preliminary analysis. Comput. Vis. Sci. 1999;2:75–83.

Gagnon L, Sakadžić S, Lesage F, Musacchia JJ, Lefebvre J, Fang Q, Yücel MA, Evans KC, Mandeville ET, Cohen-Adad J, Polimeni JR, Yaseen MA, Lo EH, Greve DN, Buxton RB, Dale AM, Devor A, Boas DA. Quantifying the microvascular origin of BOLD-fMRI from first principles with two-photon microscopy and an oxygen-sensitive nanoprobe. J Neurosci. 2015 Feb 25;35(8):3663-75. doi: 10.1523/JNEUROSCI.3555-14.2015.

Gould IG, Linninger AA. Hematocrit distribution and tissue oxygenation in large microcirculatory networks. Microcirculation. 2015 Jan;22(1):1-18. doi: 10.1111/micc.12156.

Gould IG, Tsai P, Kleinfeld D, Linninger A. The capillary bed offers the largest hemodynamic resistance to the cortical blood supply. J Cereb Blood Flow Metab. 2017 Jan;37(1):52-68.

Guibert R, Fonta C, Plouraboué F. Cerebral blood flow modeling in primate cortex. J Cereb Blood Flow Metab. 2010 Nov;30(11):1860-73. doi: 10.1038/jcbfm.2010.105.

Hillman EM, Devor A, Bouchard MB, Dunn AK, Krauss GW, Skoch J, Bacskai BJ, Dale AM, Boas DA. Depth-resolved optical imaging and microscopy of vascular compartment dynamics during somatosensory stimulation. Neuroimage. 2007 Mar;35(1):89-104.

Holmes MH. Introduction to Perturbation Methods. Springer. 2013.

Kasischke KA, Lambert EM, Panepento B, Sun A, Gelbard HA, Burgess RW, Foster TH, Nedergaard M. Two-photon NADH imaging exposes boundaries of oxygen diffusion in cortical vascular supply regions. Journal of Cerebral Blood Flow and Metabolism. 2011;31:68–81.

870 Kiani MF, Hudetz AG. A semi-empirical model of apparent blood viscosity as a function of vessel
871 diameter and discharge hematocrit. Biorheology. 1991;28(1-2):65-73.

872 Kim JH, Khan R, Thompson JK, Ress D. Model of the transient neurovascular response based on
873 prompt arterial dilation. J Cereb Blood Flow Metab. 2013 Sep;33(9):1429-39. doi:
874 10.1038/jcbfm.2013.90.

875 Kong Y, Zheng Y, Johnston D, Martindale J, Jones M, Billings S, Mayhew J. A model of the dynamic
876 relationship between blood flow and volume changes during brain activation. J Cereb Blood Flow
877 Metab. 2004;24:1382–1392.

878 Langewouters GJ, Wesseling KH, Goedhard WJ. The static elastic properties of 45 human thoracic
879 and 20 abdominal aortas in vitro and the parameters of a new model. J Biomech. 1984;17(6):425-
880 35.

881 Lauwers F, Cassot F, Lauwers-Cances V, Puwanarajah P, Duvernoy H. Morphometry of the human
882 cerebral cortex microcirculation: general characteristics and space-related profiles. Neuroimage.
883 2008 Feb 1;39(3):936-48.

884 Linninger AA, Gould IG, Marinnan T, Hsu CY, Chojecki M, Alaraj A. Cerebral microcirculation and
885 oxygen tension in the human secondary cortex. Ann Biomed Eng. 2013 Nov;41(11):2264-84. doi:
886 10.1007/s10439-013-0828-0. Epub 2013 Jul 11.

887 Lorthois S, Cassot F, Lauwers F. Simulation study of brain blood flow regulation by intra-cortical
888 arterioles in an anatomically accurate large human vascular network: Part I: methodology and
889 baseline flow. Neuroimage. 2011 Jan 15;54(2):1031-42.

890 Lucas C. An anatomical model of the cerebral vasculature and blood flow. DPhil thesis, University of
891 Oxford, 2012.

892 Murray CD. The Physiological Principle of Minimum Work: I. The Vascular System and the Cost of
893 Blood Volume. Proc Natl Acad Sci U S A. 1926 Mar;12(3):207-14.

894 Mut F, Wright S, Ascoli GA, Cebral JR. Morphometric, geographic, and territorial characterization of
895 brain arterial trees. Int J Numer Method Biomed Eng. 2014 Jul;30(7):755-66. doi:
896 10.1002/cnm.2627. Epub 2014 Jan 27.

897 Park CS, Payne SJ. A generalized mathematical framework for estimating the residue function for
898 arbitrary vascular networks. Interface Focus. 2013 Apr 6;3(2):20120078. doi:
899 10.1098/rsfs.2012.0078.

900 Payne, S.J. Methods in the analysis of the effects of gravity and wall thickness in blood flow through
901 vascular systems. In World Scientific Publishing Company themed volume on 'Biomechanical
902 Systems', ed. C.T. Leondes, 2007.

903 Payne SJ. Cerebral blood flow and metabolism: A quantitative approach. World Scientific Publishing.
904 2017.

905 Payne SJ, Lucas C. Oxygen delivery from the cerebral microvasculature to tissue is governed by a
906 single time constant of approximately 6 seconds. Microcirculation, in press.

907 Pedrizzetti G, Perktold K. Cardiovascular Fluid Mechanics. Springer. 2003.

908 Pries AR, Secomb TW. Microvascular blood viscosity in vivo and the endothelial surface layer. Am J
909 Physiol Heart Circ Physiol. 2005 Dec;289(6):H2657-64. Epub 2005 Jul 22.

910 Pries AR, Secomb TW, Gaehtgens P, Gross JF. Blood flow in microvascular networks. Experiments and
911 simulation. Circ Res. 1990 Oct;67(4):826-34.

912 Pries AR, Neuhaus D, Gaehtgens P. Blood viscosity in tube flow: dependence on diameter and
913 hematocrit. Am J Physiol. 1992 Dec;263(6 Pt 2):H1770-8. Review.

914 Pries AR, Secomb TW, Gaehtgens P. Biophysical aspects of blood flow in the microvasculature.
915 Cardiovasc Res. 1996 Oct;32(4):654-67. Review.

916 Reichold J, Stampanoni M, Lena Keller A, Buck A, Jenny P, Weber B. Vascular graph model to
917 simulate the cerebral blood flow in realistic vascular networks. J Cereb Blood Flow Metab. 2009
918 Aug;29(8):1429-43.

919 Ress D, Thompson JK, Rokers B, Khan RK, Huk AC. A model for transient oxygen delivery in cerebral
920 cortex. Front Neuroenergetics. 2009 Jun 29;1:3. doi: 10.3389/neuro.14.003.2009. eCollection
921 2009.

922 Safaeian N, Sellier M, David T. A computational model of hemodynamic parameters in cortical
923 capillary networks. J Theor Biol. 2011;271(1):145-156.

924 Schmid F, Tsai PS, Kleinfeld D, Jenny P, Weber B. Depth-dependent flow and pressure characteristics
925 in cortical microvascular networks. PLoS Comput Biol. 2017 Feb 14;13(2):e1005392. doi:
926 10.1371/journal.pcbi.1005392. eCollection 2017 Feb.

927 Shipley RJ, Chapman SJ. Multiscale modeling of fluid and drug transport in vascular tumors. Bull
928 Meth Biol. 2010;72:1464-91.

929 Stergiopoulos N, Young DF, Rogge TR. Computer simulation of arterial flow with applications to
930 arterial and aortic stenoses. J.Biomech. 1992;25:1477–1488.

931 Su SW, Catherall M, Payne S. The influence of network structure on the transport of blood in the
932 human cerebral microvasculature. Microcirculation. 2012;19:175–187.

933 Tsai PS, Kaufhold JP, Blinder P, Friedman B, Drew PJ, Karten HJ, Lyden PD, Kleinfeld D. Correlations of
934 neuronal and microvascular densities in murine cortex revealed by direct counting and
935 colocalization of nuclei and vessels. Journal of Neuroscience. 2009;29:14553–14570.

Unekawa M, Tomita M, Tomita Y, Toriumi H, Miyaki K, Suzuki N. RBC velocities in single capillaries of mouse and rat brains are the same, despite 10-fold difference in body size. Brain Res. 2010 Mar 12;1320:69-73. doi: 10.1016/j.brainres.2010.01.032. Epub 2010 Jan 18.

Vazquez AL, Masamoto K, Fukuda M, Kim SG. Cerebral oxygen delivery and consumption during evoked neural activity. Front Neuroenergetics. 2010 Jun 18;2:11. doi: 10.3389/fnene.2010.00011.

Weber B, Keller AL, Reichold J, Logothetis NK. The microvascular system of the striate and extrastriate visual cortex of the macaque. Cerebral Cortex. 2008;18:2318–2330.

Womersley, JR. Method for the calculation of velocity, rate of flow and viscous drag in arteries when the pressure gradient is known. J Physiol. 1955 Mar 28;127(3):553-63.

Zheng Y, Mayhew J. A time-invariant visco-elastic windkessel model relating blood flow and blood volume. Neuroimage. 2009;47:1371–1380.